Final report

Long-term changes in the mesosphere (LOCHMES)

Final report of the

Leibniz-Vorhaben im wettbewerblichen Verfahren (SAW-Verfahren) im Rahmen des Paktes für Forschung und Innovation 2011, Förderlinie: Qualitätssicherung

Long term changes in the mesosphere (LOCHMES)

Erich Becker, Franz-Josef Lübken, Markus Rapp[1]
Leibniz Institute of Atmospheric Physics at the University of Rostock (IAP), Kühlungsborn
[1]since 2011: DLR-Institute for Physics of the Atmosphere (IPA), Oberpfaffenhofen

1 Introduction and summary of main goals

The mesosphere and lower thermosphere (hereafter: MLT) is known as the atmospheric region between about 50 and 110 km altitude. Here, atmospheric waves and turbulence are characterized by much higher amplitudes in terms of wind and temperature variations/fluctuations than at lower altitudes. Moreover, some basic physical approximations that hold at lower altitudes are violated. For example, local thermodynamic equilibrium with regard to thermal radiation and gradient-wind balance of the large-scale flow do no longer hold. In particular, the climatological state during solstice deviates quite substantially from a hypothetical state that is determined by assuming only radiative, chemical, and convective processes in each atmospheric column (also known as the *radiatively determined state*). The dynamics in the MLT results from waves which either are generated in the troposphere (0-10 km height) or are a consequence from instabilities that are created by waves with tropospheric origin.[1] Due to upward propagation into regions of much lower density, these waves gain very high amplitudes in terms of wind and temperature variations; refraction by the prevailing winds then triggers wave breaking, transition into turbulence, and wave-mean flow interaction.

The increase of anthropogenic greenhouse gases and their effect on global climate change has been widely investigated for the troposphere. The global-mean surface temperature shows a rather small warming of 0.85 K over the period 1880 to 2012. Since the greenhouse effect ceases around 10 km, an increased CO_2 concentration leads to more efficient cooling to space in the middle atmosphere. Indeed, the atmosphere shows a long-term cooling trend above about 10 km. This global change of the atmosphere is particularly large in the height range from about 50 to 75 km. Due to the dynamical control of the MLT by the troposphere and its sensitivity to the CO_2 concentration, the MLT is sometimes considered as an indicator for climate change.

This project has focused on the coupling mechanisms between the lower and middle atmosphere. Beyond basic research to explore the middle atmosphere and especially the MLT, the overall motivation has been to probe the mesosphere as a possible indicator for climate variability and thereby to better distinguish between natural and anthropogenic changes of the climate system. We have proposed to make various efforts in order to improve the mechanistic concept of a climate model, and to further facilitate our ground-based measurement techniques in order to better quantify the mean state and its variability. As a particular focus we have proposed to analyze the quasi-biennial oscillation (QBO) and the Holton-Tan mechanism along with its dependence on the solar cycle and its vertical extent into the MLT in terms of interhemispheric coupling. In the following we briefly discuss the achieved progress regarding methodological developments and understanding of geophysical processes.

---

[1]Thermal tides are partly forced by absorption of solar insolation in the stratospheric ozone layer.

2 Progress and results

2.1 Technical developments

2.1.1 Global circulaton model

During the course of the project, the Kühlungsborn Mechanistic general Circulation Model (KMCM) has been further developed regarding the following aspects.

The new method for computation of radiative transfer developed at IAP (Knöpfel and Becker, 2011) has been extended as described recently in Becker et al. (2015). Unlike to comprehensive climate models where different radiation schemes are used for different altitudes regimes and the resulting radiative heating rates are merged, the idealized scheme employed in the KMCM is based on a flux computation and extends continuously from the surface to the top of the atmosphere.

The model has been equipped with parameterizations of gravity waves (GWs). A scheme for orographic GWs has been developed (Wolf, 2013). The method is based on the ideas of McFarlane (1987) but uses a more general dispersion relation and includes the full scale interaction between the mean flow, parameterized GWs, and parameterized turbulent diffusion. These ideas follow the principles that are implemented also in the parameterization of non-orographic GWs (Becker and McLandress, 2009). In particular, the KMCM takes the energy deposition of GWs consistently into account. This is often not the case in comprehensive climate models though being important for energetic consistence.

A new tracer transport scheme that advances the method used in the Canadian Middle Atmosphere Model (CMAM) has been developed by Schlutow et al. (2014). It includes 1) a continuous tracer functional that is represented in spectral space, 2) a mass correction that takes advection plus physical sinks and sources into account, and 3) a rigorous application of the model's nonlinear vertical and horizontal diffusion to tracers. These measures allow for accurate conservation of mass and energy regarding the moisture cycle.
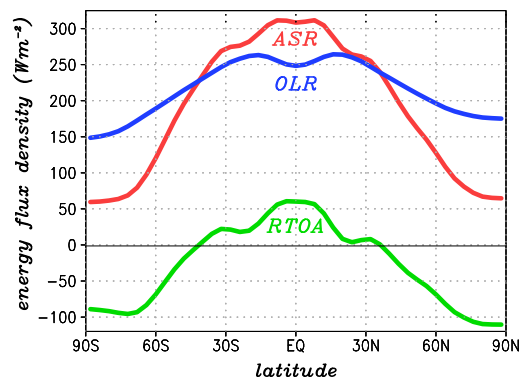

Figure 1: Simulated latitude-dependence of the climatological-mean radiation budget at the top of the atmosphere: Absorbed solar radiation (ASR, red curve), outgoing long-wave radiation (OLR, blue curve), and net downward radiation (RTOA=ASR–OLR, green curve). The global mean of both the ASR and OLR is about 233 W m^{-2} while the reflected radiation amounts to 107 W m^{-2}. These numbers are well comparable to observational estimates. The some holds for the radiative energies absorbed by the atmosphere and at the surface, as well as for the latent and sensible heat fluxes at the surface. The imbalance in the mean RTOA is only -0.2 W m^{-2}; it results from slight aliasing errors in the surface budget and the moisture cycle.

The newly implemented moisture cycle employs a simple convection scheme that relaxes temperature and moisture to reference profiles that correspond to piecewise moist-adiabatic lapse rates. Convection reaches from the lowest full model layer up to the highest layer where the actual temperature falls below the reference temperature and the specific humidity is larger than the reference value. The relaxation times are specified by the mass-flux method. Large-scale condensation is applied above each convective column. In addition, the specific humidity is relaxed to zero with a

time constant of one year in order to balance the moisture flux into the middle atmosphere. We do not consider re-evaporation and assume that all condensates precipitate.

The climate model version of the KMCM as developed during the course of LOCHMES also includes the full surface energy budget in terms of a simple slap ocean model with prescribed lateral oceanic heat flux. It preserves energy because each energy conversion is formulated in an energy conserving way. This is usually not possible in complex climate models. Accordingly, an equilibrated radiation budget at the top of the atmosphere, the co-called RTOA (see Fig. 1), is usually achieved by tuning as discussed by Lucarini and Ragone (2011). In the KMCM, equilibrated global climatological global means of the RTOA, surface budget, and water-vapor budget are simulated independently from adjustable model parameters.
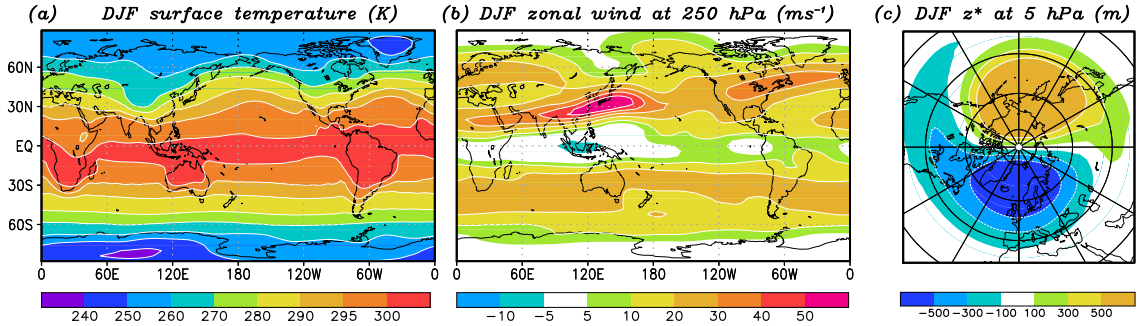

Figure 2: Simulated horizontal structure during the NH winter season (December to February). (a) Surface temperature (K). (b) Zonal wind (m s^{-1}) at 250 hPa. (c) Longitudinally varying component of the geopotential height (m) at 5 hPa.
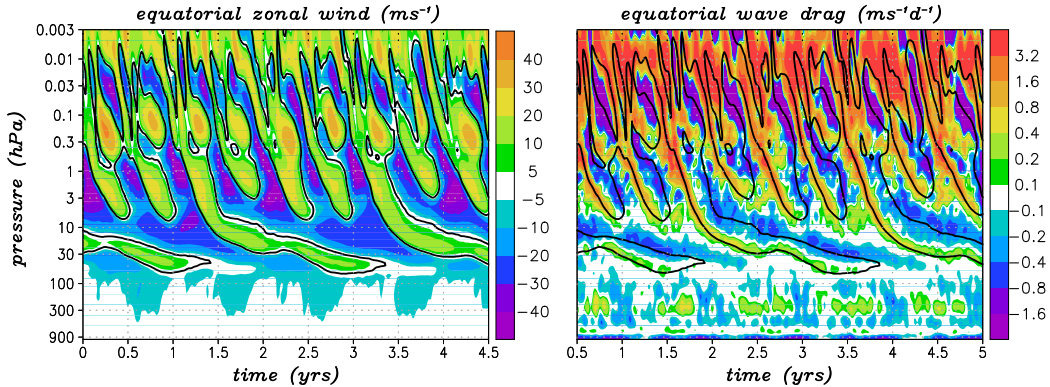
.

Figure 3: Self-generated QBO in the KMCM: Equatorial zonal-mean zonal wind (left) and Eliassen-Palm flux divergence of resolved waves plus non-orogragraphic gravity-wave drag (right). The zero-wind line in inserted by a black contour in each panel. The QBO is driven by the combination of resolved and parameterized waves.

The KMCM has been specified with three different spatial resolutions that all extend from the surface up to about 125 km. The first one is a conventional, i.e., triangular truncation at a horizontal wavenumber of 32 and 70 full atmospheric layers (T32L70). Figure 2 shows some simulated horizontal structures regarding the surface temperature and stationary waves during northern hemispheric winter. The second setup is T42L115 and uses an enhanced vertical resolution in the stratosphere in order to allow for a self-generated QBO (Fig. 3). Note that this requires an adequate simulation of resolved tropical waves along with the proper tuning of the parameterization of non-orographic gravity waves. (e.g., Schmidt et al., 2010). The third model setup uses the same high resolution as in Becker (2009), i.e., T120L190, as well as the same parameterization of turbulent diffusion in order to simulate drag and dissipation due to resolved gravity waves in a self-consistent fashion (see Fig. 4). This model version has been consolidated only recently. It is one out of two cli-

3

mate models world-wide that extend into the lower thermosphere and explicitly simulate a realistic summer-to-winter-pole residual circulation in the MLT that is driven by resolved gravity waves.[2]
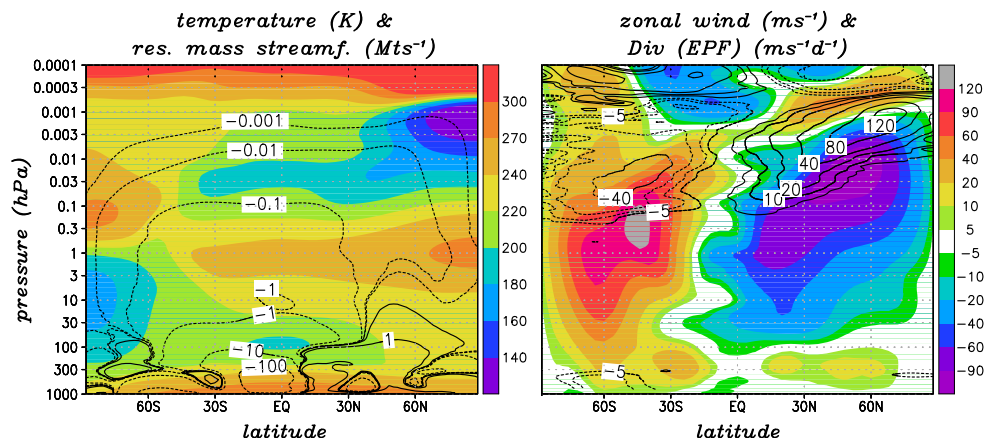

Figure 4: Zonal-mean model climatology for July obtained with the KMCM at T120L190 resolution. Gravity-wave effects are due to only resolved scales and show a realistic Eliassen-Palm flux (EPF) divergence in the northern summer mesosphere along with a realistic strength of the residual circulation in the mesosphere

2.1.2 Derivation of the three-dimensional wind field from satellite measurements

The investigation of the long-term changes in the middle atmosphere requires knowledge about the three-dimensional (3D) wind field. Corresponding data are usually available through model simulations or extrapolated data assimilations, and are subject to various uncertainties. This limitation arises from the incomplete horizontal, vertical, or temporal coverage of direct wind measurements by standard radiosondes (limited to 30 km), rocket soundings, satellites, and ground-based methods. Hence, validation of simulated global wind fields against direct observations is mostly impossible. As an alternative, so-called balanced wind components have been derived from satellite-borne temperature measurements (e.g., Manney et al., 2008; Gabriel et al., 2011a). However, these winds are uncertain when the flow deviates from geostrophic balance, and they capture neither the residual circulation, the circulation in the tropics, nor gravity waves. We have developed a new two-step method for deriving daily-mean 3D wind fields in the middle atmosphere from Aura/MLS temperature and Aura/MLS water vapor data provided by NASA. Our algorithm includes 1) the derivation of winds from temperature and geopotential using standard balance equations in quasi-geostrophic approximation, and 2) an optimization of the daily-mean 3D wind vectors by iterative adjustment to the day-to-day variations in the transport of water vapor (by inversion of the tracer transport equation, considering that water vapor is a nearly inert tracer in the stratosphere and mesosphere) which provides an estimate of the unbalanced wind components. The derived daily-mean winds agree very well with ground-based lidar wind measurements of IAP (Baumgarten, 2010). The new dataset has become an efficient tool to understand and validate long-term variability in model simulations and assimilated data sets.

2.1.3 Simulation of ice clouds in the summer mesopause region

The formation of ice layers is calculated with the LIMA[3]/Ice. As an improvement we developed a data-interface which allows us to connect the ice model to any data of mesospheric background conditions. Such background fields may be provided by either observations or by model data. In

---

[2]The other model is based on the Kanto model (Watanabe and Miyahara, 2009) and can only be run for short time intervals on the Earth Simulator in Japan.

[3]LIMA=Leibniz-Institute Middle Atmosphere model

this study we use LIMA/Ice in combination with the LIMA model output as has been described in detail in Lübken et al. (2013).

Figure 5 shows the observed long-term dependencies of CO_2 and O_3, as well as of solar activity described by Lyman-alpha radiation (Ly_α) for the period 1961-2013. These variations are prescribed in LIMA simulations in order to calculate trends in the MLT. Daily values of Ly_α flux in units of 10^{11} photons/(cm^{2}s) are our proxy of solar activity. Long-term variations in trace gases cause temperature trends in the mesosphere. Temperatures vary non-uniformly in time in the MLT, mainly due to the influence of stratospheric O_3 (Berger and Lübken, 2011). As a consequence, the formation of PMCs modeled by LIMA/Ice is affected by changing long-term thermal and dynamical conditions.
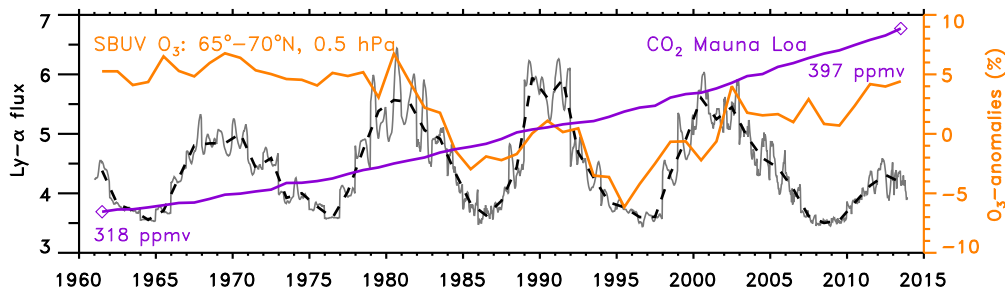

Figure 5: Monthly July averaged trace gas distributions of CO2 data as measured at Mauna Loa (from http://www.esrl.noaa.gov/gmd/ccgg/trends), ozone data as relative anomalies at 0.5-0.7 hPa from 1979 to 2013 as measured by the solar backscatter ultraviolet (SBUV) satellite instruments (from http://acd-ext.gsfc.nasa.gov/Data_services/merged/) and from the latest World Meteorological Organization (WMO) report for 1961-1978, and solar activity by daily Ly_α fluxes in the period 1961–2013 (from http://lasp.colorado.edu/lisird).

The LIMA/Ice simulates the formation of mesospheric ice layers by transporting 40 million meteoric dust (smoke) particles acting as potential condensation nuclei (CN) in the cold summer mesopause region at high latitudes. Several microphysical processes are included such as heterogeneous nucleation, growth, sublimation, sedimentation, particle diffusion, and particle temperature (Lübken and Berger, 2011). The model domain of LIMA/Ice is defined poleward of latitudes of $37°$ at an altitude range between 77.8 km and 94.1 km. The size distributions of the CNs is prescribed according to Hunten et al. (2009) and comprises particles with radii between 1.2 nm and 3.7 nm that are attributed to 5 size classes of 0.5 nm width. The distribution of smoke particles per bin are is: 86.5 % (1.2–1.7 nm), 11.7 % (1.7–2.2 nm), 1.7 % (2.2–2.7 nm), 0.2 % (2.7–3.2 nm), and 0.02 % (3.2–3.7 nm). The initial seeding domain of smoke particles extends from 83 km to the mesopause and from $55°$ to $90°$N. When individual smoke particles arrive at the domain boundaries, they are relocated into randomly chosen locations within the initial seeding domain. This procedure provides a quasi-steady state of permanent available smoke particles during the total PMC season. Fur further details see Kiliani (2014).

LIMA/Ice starts the simulation of each PMC season in the period 1961–2013 in the northern hemisphere (NH) at 20 May. We initialize LIMA/Ice with a constant latitude/longitude/height distribution of H_2O that is constant on pressure levels at the beginning of each seasonal simulation. Then, water vapor is exposed to photo-dissociation by varying Ly_α radiation, transport, and turbulent diffusion. It interacts with ice particles which leads to redistribution of H_2O by freeze drying until the season ends at 20 August. Figure 6 shows a typical snapshot of the ice particle distribution modeled by LIMA/Ice for 10 July, 2008 at 24:00 UT. In Figure 6a the radii of all ice particles which are located in the model subdomain at $68°$–$70°$N latitude and $50°$–$60°$E longitude, are plotted. Ice particles reach maximum radii of about 40 nm near 83 km, whereas the largest number of ice particles is located near 89 km. The number of model particles (N = 96170) being a fraction of the total of 40 million model particles is converted to a physical unit of number density

per cm^3 which is shown in Figure 6b. Details of this conversion procedure have been described in Kiliani (2014). Furthermore, we show the mean, median, and the effective radius of ice radii, see Figure 6b.
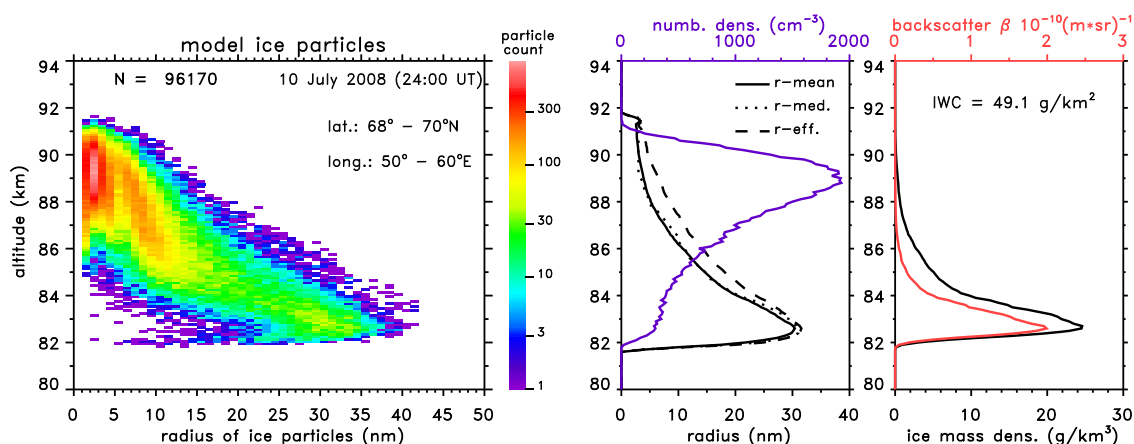

Figure 6: (a) Distribution of ice particle modeled by LIMA/Ice. (b) Number density and mean radius of the distribution. (c) Backscatter in lidar geometry at 532 nm, ice water/mass density (IWD) and ice water content (IWC).

Ground-based lidars measure backscatter intensities of NLC. We compute from the original ice particle distribution (Figure 6a) a model backscatter profile which is shown in Figure 6c. Since Mie-scattering is proportional to $n \cdot r^a$, with the exponent a being in the range of 5–6, the backscatter profile exhibits a sharp maximum at an altitude where the radii maximize. Hence, the altitude z_{max} of backscatter maximum is a very suitable parameter to quantify the altitude of PMCs (Baumgarten et al., 2012). Our model results of mean values and variabilities for ice particle altitudes and radii agree in general with observations (e.g., Baumgarten and Fiedler, 2008; von Savigny et al., 2005).

2.1.4 Lidars

Lidars have experienced significant technological developments in recent years. This concerns, for example, the capability to measure number densities and temperatures with high temporal and spatial resolution from the ground up to the lower thermosphere. Recently lidars were developed to measure wind profiles in the lower and middle atmosphere. These measurements are now available even during full daylight which requires special attention for long-term studies to ensure a homogeneous and consistent data set. Several technical developments were designed, tested and implemented in order to achieve daylight-capability. This includes, for example, the development of ultra-stable etalons used to suppress solar photons, or the beam stabilization for the outgoing laser-beam which needs to match the field-of-view of the telescope (*Gerding et al.*, 2015; *Eixmann et al.*, 2015). The latter must be very small (some tens of micro-radian) in order to monitor the sky only in a very limited range around the laser beam. In the context of LOCHMES, long-term observations of temperatures, mesospheric ice layers (known as 'noctilucent clouds', NLC), and metal layers in the upper mesosphere/lower mesosphere (UMLT) are of particular importance. We deduce ice particle parameters from lidar NLC detection at various wavelengths. Our respective data base is the largest and most detailed worldwide.

Metal layers are sensitive to photochemistry and can therefore be used to study the impact of long-term solar irradiance variation, e.g., during a solar cycle, or depletions due to very low temperatures and/or attachment to ice particles (*Viehl et al.*, 2015). Regarding metal number densities, we have observed and analyzed data from our stationary lidar in Kühlungsborn for the years 2002 to 2012. Systematic data processing for this period of 10 years included the generation of a reference data-set for validation of satellite observations, as well as the specification of seasonal variations and trends.

Currently we are preparing a paper on long-term variations of the potassium layer, including our own lidar observations and data from the ODIN satellite.

2.1.5 Radars

Ground-based measurements for winds have been derived from the unique, narrow beam medium frequency (MF) Doppler radar which is located on the island of Andøya (69°N, 16°E). The benefits of this radar, called *Saura*, are continuous and high-quality measurements over a broad height range with high temporal and vertical resolution during all seasons. The Saura radar transmits and receives electromagnetic signals with a Mills Cross antenna of 29 crossed dipoles at a frequency of 3.17 MHz (Singer et al., 2008). Two coplanar tilted radar beams are transmitted successively in different spatial directions with a fixed off-zenith angle of 6.8°. For any pair of opposite radar beams, the radial wind velocity is measured within 2 minutes. This means that the measurement for four spatial directions (two coplanar beam measurements perpendicular to each other) takes 4 minutes. This is the temporal resolution for the analysis of horizontal wind components. The vertical range is from about 60 to 100 km height with a resolution of 1 km (for further details see Placke et al., 2015a).

2.2 Geophysical results
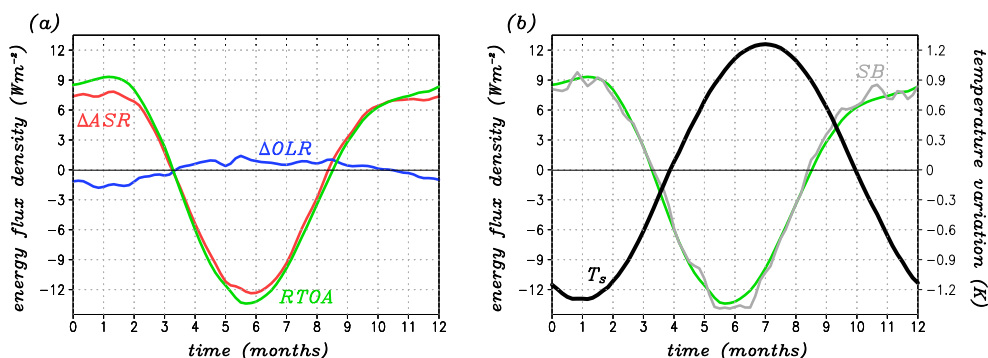
2.3 Annual cycle and variability modes

Figure 7: Simulated annual variations of the global mean radiation budget at the top of the atmosphere (ASR, OLR, and RTOA), the global-mean surface budget (SB), the global-mean surface temperature (T_s).

Annual variation of the radiation and surface energy budgets

In a preliminary study, the T32L70 version of the KMCM has been used to study the regular annual cycle of the RTOA, the surface budget, and the global-mean temperature (see Fig. 7). This study was inspired by the fact the there is a significant annual variation of the outgoing long-wave radiation (OLR) that is out of phase with the absorbed solar (ASR).[4] Such an effect was also found in an observational analysis of Fasullo and Trenberth (2008), but has not yet been analyzed or confirmed on the basis of a global climate model. The KMCM shows that the annual variation of the OLR is caused by a corresponding variation of the global-mean surface temperature, T_s, of about ±1.5 K, which is also visible in reanalyses (not shown). However, the planet is coldest and the OLR is minimum during northern hemispheric winter when the ASR maximizes. This unexpected behavior is caused by the different distributions of land and ocean surfaces in the two hemisphere, with the vast ocean surfaces in the southern hemisphere having a much higher heat capacity than the continents in the northern hemisphere. In particular, when the surface cools in the global mean during northern hemispheric winter, it nevertheless stores heat. The reverse hold during northern summer. This mechanism provides a new view on the observed positive imbalance

---

[4]The ASR latter undergoes a strong annual cycle of about ±10 W m^{-2} because of orbital eccentricity.

of the RTOA of about $1\,\mathrm{W\,m^{-2}}$ that has been observed during the last 15-20 years along with a stagnation of global warming (so-called hiatus). The hiatus is presumably caused by heat storage in the deep ocean due to natural variability (Meehl et al., 2011) such that the *hiatus occurs despite the imbalance* (Hansen et al., 2005). The aforementioned simple and very robust result for the annual cycle suggests, however, that the imbalance is at least partly *caused* by the hiatus. We submitted a corresponding paper to the Journal of Climate which was rejected because of pointing on this possible implication. We are currently working on a new and improved manuscript (Becker, Knöpfel, and Bothe, 2015, Annual cycle of the global radiation budget in an idealized climate model, in preparation for publication in *Nonlinear Processes in Geophysics*). We have proven that the middle atmosphere does not play a role in this mechanism, even though the radiation absorbed and emitted by the middle atmosphere amounts to about $20\,\mathrm{W\,m^{-2}}$, and even though temperatures undergo strong annual variations associated with the residual circulation.
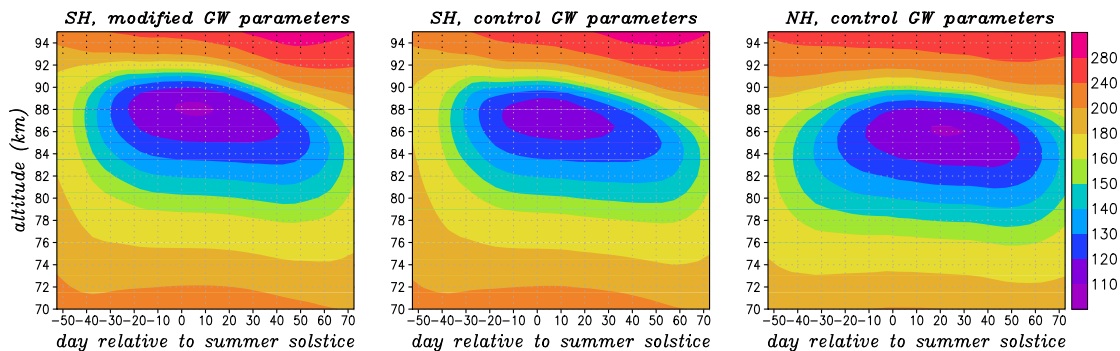

Figure 8: Temporal evolution of the temperature around the summer polar mesopause for the (a) southern hemisphere when using modified launch level parameters for gravity waves, (b) and (c) for the southern and northern hemisphere, respectively, when using the same launch level parameters in either hemisphere.

Hemispheric differences in the polar summer mesopause

Inspired by new measurements performed with the IAP resonance lidar at the station of Davis at Antarctica (e.g., Lübken et al., 2014), we have performed a model study that explains the observed hemispheric differences in the seasonal cycle of summer polar mesopause in terms of *intrahemispheric coupling* and *interhemispheric coupling* (Becker et al., 2015). A consequence is that the mechanism of *interhemispheric coupling*, which has been in the focus of this project at its outset, must be complemented by a corresponding *intrahemispheric coupling* in order interpret recent observational knowledge about the dynamics of the MLT. Figure 8 shows the simulated temporal evolution of the summer mesopause in the two hemispheres. It is important to note the observed behavior can be much better explained when the launch level parameters in the southern hemisphere are modified compared to those in the northern hemisphere such as to enhance the importance short-period gravity waves that have better vertical propagation conditions (see also Lübken et al., 2015). Generally, as is evident from panel b and c in Fig. 8, the southern mesopause sets in at higher latitudes and then propagates downward when compared to the northern hemisphere. The combination of IAP's unique observational results combined with modeling activities demonstrates how models can be validated and constraint using ground-based measurements.

Interaction of thermal tides with gravity waves (GWs) and the mean flow

Thermal tides are the strongest waves in the MLT. They are commonly studied regarding their morphology (amplitudes, phases) and dynamics. They are known to be strongly influenced by GWs (Ortland and Alexander, 2011). On the other hand, their role in driving or modulating the general circulation in the MLT has only rarely been studied. Tides are generally resolved in middle atmosphere circulation models. Even though their interaction with parameterized GWs is usually subject to oversimplifications (Senf and Achatz, 2011), general aspects can be deduced from

conventional models with parameterized GWs. We have used the KMCM with T32L70 resolution in order study the influence of thermal tides on the general circulation. To this end we have performed a sensitivity study analogously to that presented in Becker (2012). More specifically, we compare a control simulation to a perturbation run in which all short-wave radiative heating rates were substituted by their zonal means, thereby neglecting the generation of thermal tides due to absorption of solar insolation by ozone and tropospheric water vapor. The main results of this sensitivity experiment is that thermal tides 1) give give rise to substantial energy deposition and 2) cause a downward shift of the GW drag and energy deposition in the MLT (see Fig. 9). The first effect is usually ignored in comprehensive models since the frictional heating due to momentum diffusion is neglected. The second effect is inherently included in comprehensive climate models, along with the obvious deceleration due to tides in the thermosphere.[5] An important consequence of these interdependencies is that the tuning of GW parameters crucially depends on the details of the simulated tidal activity. Thus, studies about climate variability in the MLT must not only take the variations of GW activity and GW effects into account, but the corresponding variations of thermal tides as well. As long as stratospheric ozone trends are small, tidal variations are largely due to changes in tropospheric water vapor and GW sources.
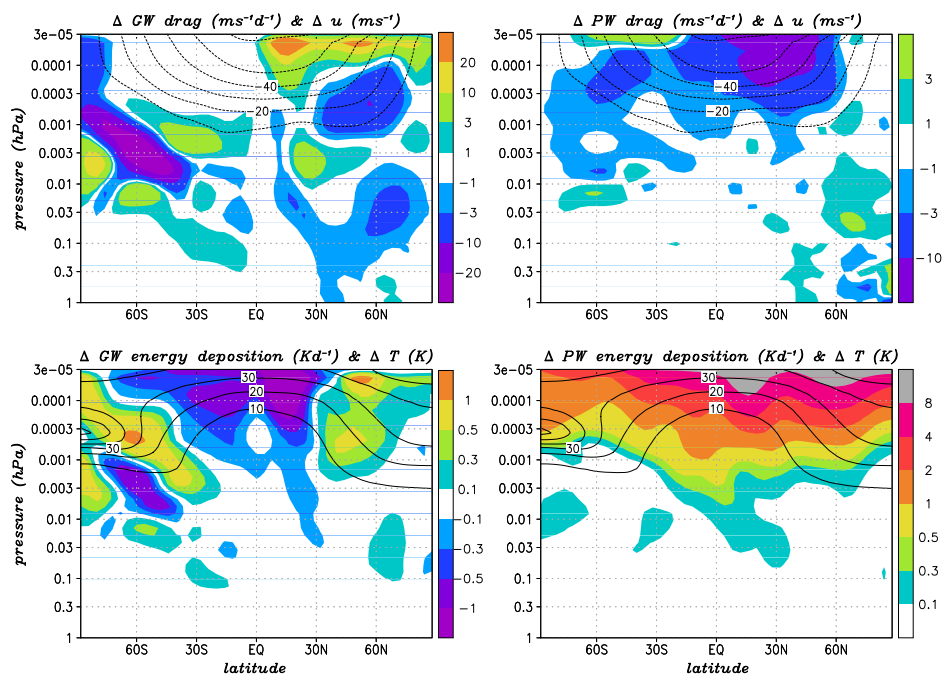

Figure 9: Model response of the zonal-mean climatology during January to thermal tides. The contours in both upper panels show the zonal-wind response, which is characterized by a substantial deceleration, while contours in the lower panels show the temperature response, which exhibits a substantial heating of the thermosphere. Colors in the upper panels show the changes of the wave driving with regard to gravity waves (GW drag, left) and planetary waves (including tides, PW drag, right). Colors in the lower panels display the changes in the energy deposition due to gravity waves (left) and planetary waves (including tides, right).

Extension of the Holton-Tan effect into the MLT

The T42L115 version of the KMCM simulates a self-generated QBO (see Sec. 2.1.1, Fig. 3) and reproduces the Holton-Tan effect during January in line with the analysis of Baldwin and Dunkerton (1998). As is shown in Fig. 10, the Holton-Tan effect as simulated with the KMCM extends into the MLT and shows the interhemispheric coupling pattern.

We have performed an analysis of the Holton-effect in the MLT using the CMAM30 data set (for references see Fomichev et al., 2002; McLandress et al., 2013), as well as MLS satellite data. Results

---

[5]The Eliassen-Palm flux divergence of thermal tides is negative in regions of wave breaking.
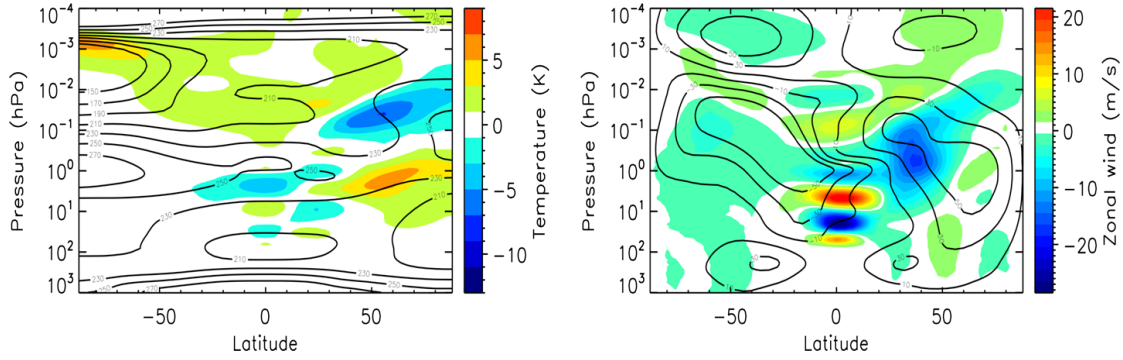
Figure 10: Holton-Tan effect during January as simulated with the KMCM. Left: Temperature response for the composite difference of easterly QBO minus westerly QBO. Right: Corresponding zonal-wind composite difference. The contours in each panel give the January zonal-mean climatology with contour intervals of 20 m/s and 20 K.

have recently been published in Matthias and Becker (2015). When we do not discriminate the different phases of the 11-year solar cycle, the Holton-Tan effect is well visible only in the winter stratosphere and winter mesosphere, but does not extend to the summer polar mesopause as would be expected from interhemispheric coupling (Fig. 11a). The most likely reason is that the long-term variation of absorption of solar radiation around the summer stratopause presumably causes some intrahemispheric coupling that is analogous to the model response to solar proton events (Becker and von Savigny, 2010). When sorting the data with respect to the phases of the solar cycle (Fig. 11b-d), we find a pronounced signal for solar maximum conditions that is consistent with the KMCM result (computed for constant solar activity). The KMCM (see Fig. 10) produces a stronger heating in the thermosphere for QBO-east minus QBO-west when compared to the CMAM30 result for solar maximum . The reason is that tidal amplitudes, and hence also the tidal energy deposition, become stronger for weaker gravity wave amplitudes in the MLT, as is the case for the easterly phase of the QBO. As mentioned above, the energy deposition is not fully included in other models.
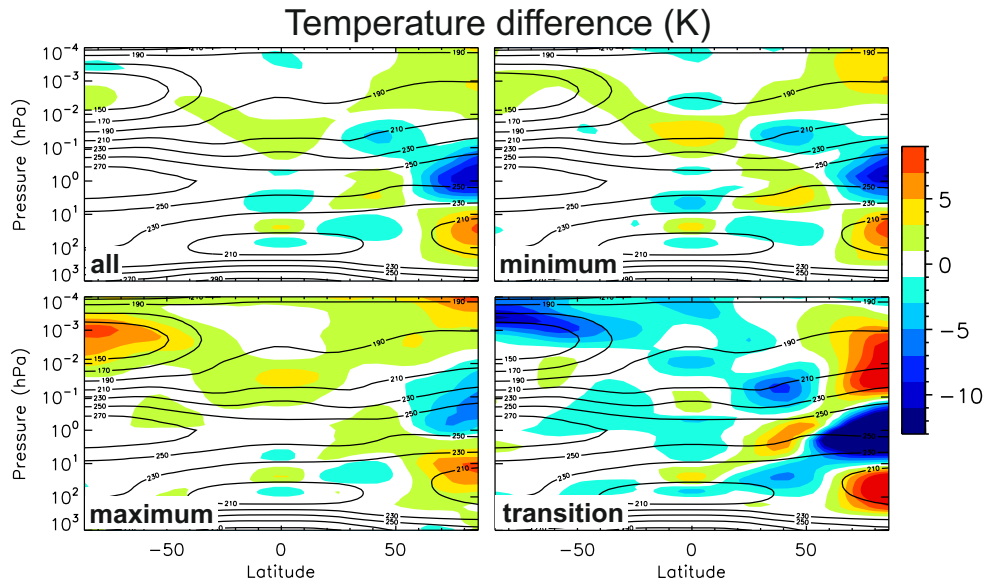

Figure 11: Holton-Tan effect (i.e., composite difference between the easterly and westerly phase of the QBO) with respect to temperature during January as deduced from the CMAM30 data set extending from 1979 to 2009. a) Complete time series. b) For solar maximum only. c) For solar minimum only. d) During the transition periods. The contours in each panel display the mean January temperature with a contour interval of 20 K.

An extension of the HT effect into the MLT via interhemispheric coupling shows up also during solar minimum. Surprisingly, during the transition phase between solar minimum and maximum the situation is more complicated and even reversed regarding the signal in the summer MLT. This phenomenon is presently being investigated. A further study on the role of interhemispheric coupling in the MLT has recently been published by Karlsson and Becker (2015).

2.3.1 QBO and three-dimensional residual circulation

The effect of the QBO on the northern winter hemisphere includes not only weaker westerlies in the stratosphere but also a variation in the structure of quasi-stationary planetary waves. The zonal wavenumber 1 is particularly pronounced during the easterly phase of the QBO, whereas wavenumber 2 dominates during the westerly phase. This observational finding has not been understood. We have analyzed the related dynamical processes in long-term simulations with the high-altitude circulation and chemistry model HAMMONIA (e.g., Schmidt et al., 2010) and ERA-Interim reanalysis (provided by the ECMWF). This has revealed significant discrepancies between HAMMONIA and ERA-Interim concerning the effects of both the 11-year solar cycle and the QBO (Gabriel et al., 2011b). We have then investigated the stationary waves with the new dataset of 3D wind fields derived from Aura/MLS satellite data as described in Sec. 2.1.2. The diagnosis furthermore includes the novel concept of the 3D residual circulation (Kinoshita et al., 2010; Sato et al., 2013). As an example, Fig. 12 shows January ensemble means of the vertical residual wind, w_{res}, and water vapor at 60°N for QBO-east (upper panels) and QBO-west (lower panels). For all datasets, w_{res} exhibits a pronounced wavenumber 1 during QBO-east (with downwelling towards the centre of the stratospheric polar vortex over Northern Europe/West-Siberia) and a pronounced wavenumber 2 during QBO-west (with a second branch in the downwelling over the North Pacific/North America region). Corresponding patterns are also seen in the water vapor mixing ratio because the 3D residual circulation represents, to a first order, the 3D-structure of the time-mean tracer transport.
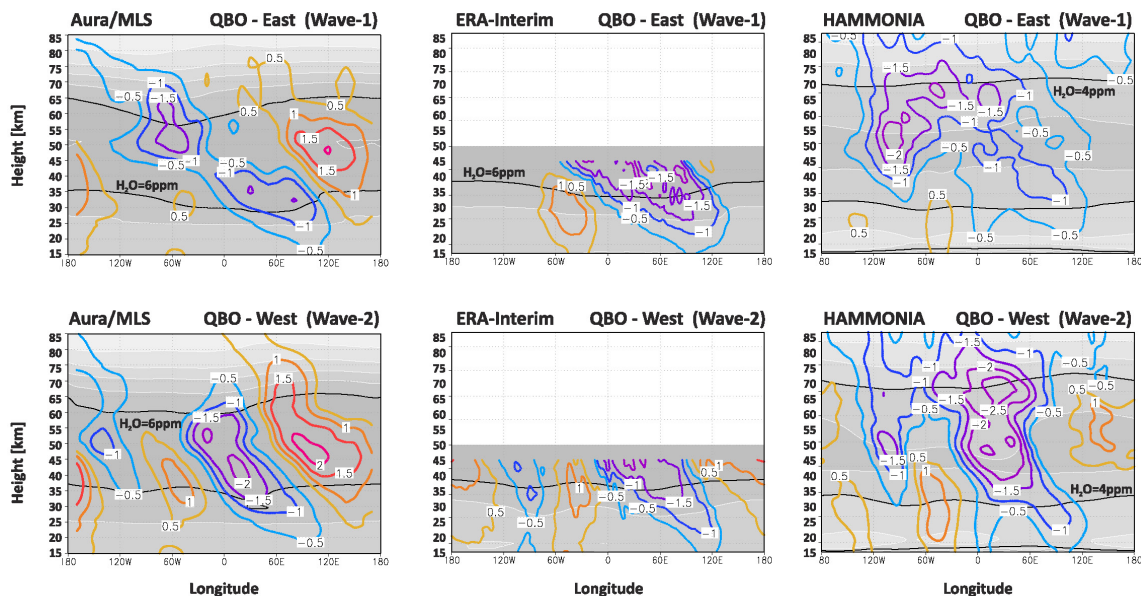

Figure 12: Vertical residual wind w_{res} (contours, unit cm/s) and water vapor mixing ratio (shaded, unit ppm, only the thick black line is labeled). Left: Aura/MLS. Middle: ERA-Interim. Right: HAMMONIA. Shown are ensemble means of 3 Januaries at 60°N for QBO-east (upper panels) and QBO-west (lower panels).

There are significant differences between the datasets. The ERA-Interim deviate from Aura/MLS due to the lack in observed winds for altitudes above 30 km, and because the upper boundary of the assimilation model is at 0.1 hPa such that resolved waves must be strongly damped beneath that
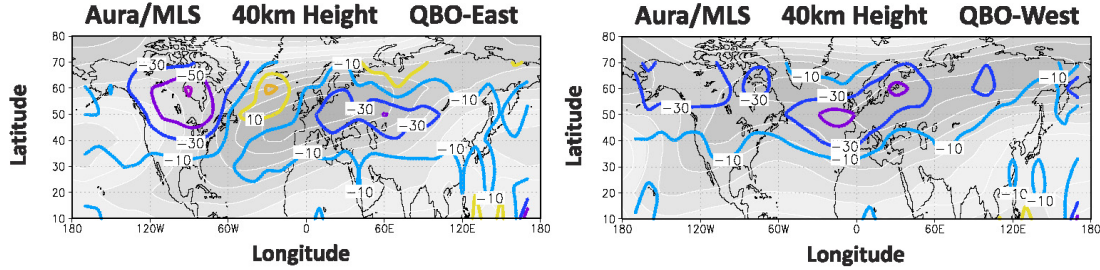
Figure 13: Wave-flux divergence that balances the Coriolis force associated with the residual zonal flow (contours, unit m/s/d) and zonal wind (shaded, interval 10 m/s, not labeled) at 40 km for QBO-east (left) and QBO-west (right) for the 3D wind fields derived from Aura/MLS

level. The HAMMONIA result is characterized by too strong transient waves at the expense of the stationary waves, which is a typical bias in circulation models (the corresponding differences in the balanced fields are even stronger, which is not shown here). On the other hand, the QBO-signal propagates into the upper mesosphere due to the modulation of parameterized gravity waves by quasi-stationary planetary wave. This feature is not sufficiently captured by the wind fields derived from Aura/MLS because gravity-wave effects are not yet introduced into the algorithm. Accurate formulations of these processes are quite challenging and subject to another ongoing project.

Figure 13 shows the wave flux divergence that drives the zonal flow in the framework of the 3D residual circulation together with the zonal wind at 40 km height for Aura/MLS. During QBO-east (left panel) we find strong transient wave activity over North America which partly suppresses the planetary wave generation by the Rocky Mountains. This is the reason why during QBO-east a predominant wavenumber 1 pattern occurs in the westerly flow. On the other hand, during QBO-west (right panel) we find a more zonally uniform transient wave activity such that the Rocky mountains fully contribute to the planetary Rossby-wave generation, leading to a pronounced zonal wavenumber 2 in the westerly flow.

Overall, these results provide new evidence how the QBO modulates the quasi-stationary planetary waves as well as the 3D residual circulation. We have also proposed a new and promising opportunity to compute observation-based global wind fields in the middle atmosphere. In addition, our analysis has revealed an important top-down effect of the QBO-induced surface-high anomaly over Northern Europe/West-Siberia during winter (not shown). Such an effect is caused by variations in the downwelling branch of the 3D residual circulation, thus emphasizing the active role of the changes in the middle atmosphere for regional climate conditions.

2.3.2 Ice clouds and trends: Comparison of modeled trends with SBUV observations

The SBUV satellites measure the albedo of polar mesospheric clouds (PMCs) that can be used to estimate ice water content (IWC) and the ice mass density (IWD) integrated over the vertical column. The IWD profile is very similar to the backscatter profile. Hence, a large part of the IWC stems from the height region near 83 km where the IWD maximizes. For this reason, this altitude region is of special interest for our PMC trend study.

Trends have been investigated for all ice parameters such as maximum backscatter β_{max}, number density and mean radius at the height of β_{max}, and IWC. We have validated our modeled IWC trends against long-term variations in the IWC derived from SBUV measurements (Hervig and Stevens, 2014; DeLand and Thomas, 2015). In Fig. 14 we show relative seasonal means of the IWC. The length of the PMC season to calculate model averages is the same as in the SBUV analysis with a range from 20 days before solstice to 55 days after solstice. Seasonal means of IWC data from SBUV are available at http://sbuv2.gsfc.nasa.gov/pmc/v4. For the latitude band 64°- 74°N, the LIMA/Ice IWC values (gray dots) are in nice agreement with IWC means taken from SBUV (red dots). We have performed a multiple regression analysis including a linear trend and a solar

cycle signal to the LIMA/Ice and SBUV data for the period 1979–2013. Positive but insignificant trends are found in both cases. The trend values for LIMA/Ice ($m = 1.7\pm1.7$ g km^{-2}/dec) and for SBUV ($m = 1.4\pm1.7$ g km^{-2}/dec) agree almost perfectly. When considering the entire period from 1961 to 2013, only model data are available. For this period, the multiple regression analysis results in a trend of $m = 3.0\pm0.7$ g km^{-2}/dec which is positive and highly significant. Hence, a period of 35 years might be too short to estimate significant trend signals in PMC observations whereas 50 years should be sufficient.
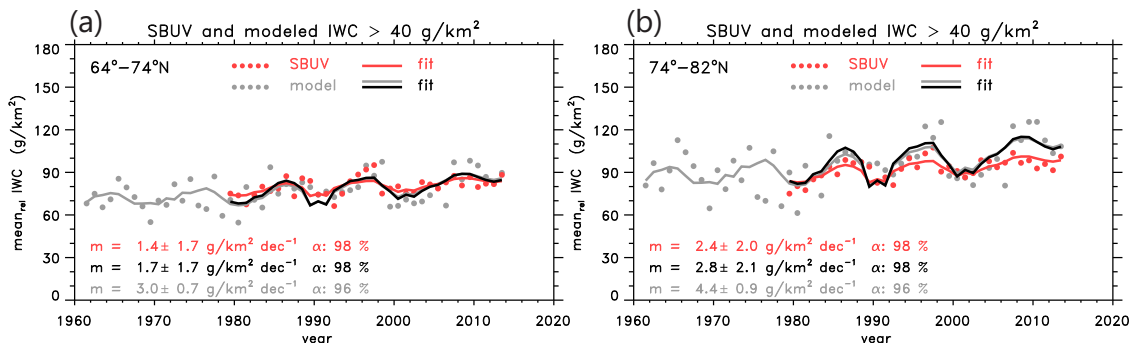

Figure 14: Comparison of LIMA/Ice relative seasonal means of IWC with satellite observations from SBUV. (a) IWC from the LIMA/Ice model (gray dots) for 64°- 74°N, similar to the bins chosen for SBUV observations (red dots). The LIMA/Ice curves represent multiple regression fits consisting of a constant, a straight line with a trend value m, and a solar cycle function for the period 1961–2013 (gray curve) and for the period 1979–2013 (black curve. The SBUV curve presents the corresponding regression fit for the period 1979–2013 (red curve). All modeled seasonal mean values are determined by applying a threshold of 40 g km^{-2} which is the threshold imposed also by the SBUV instrument. (b) Same, but for the latitude range at 74°- 82°N.

When we investigate the latitude band 74°- 82°N (Fig. 14b), the modeled relative means of IWC are slightly larger than SBUV relative means and the regression functions differ slightly. For the period 1979–2013, trends derived from both model and satellite data show significant values of $m = 2.8\pm2.1$ g km^{-2}/dec and $m = 2.4\pm2.0$ g km^{-2}/dec, respectively, and again agree nicely within their error bars. For the entire period 1961–2013 the model trend becomes slightly larger and even more significant, $m = 4.4\pm0.9$ g km^{-2}/dec.

DeLand and Thomas (2015) also evaluated changes in ice mass of PMC at mid latitudes 50°N–64°N. They found a zero trend of $m = 0.00\pm0.06$ g km^{-2}/dec for the period 1979–2013 which can be shown to be consistent with our simulation (not shown). A further trend analysis based on SBUV IWC data has been recently published by Hervig and Stevens (2014). In this study the authors estimate IWC trends using again multiple regression (linear plus solar forcing) during 1979-2013 for 64°N– 74°N. The result is a small positive trend (insignificant) in relative seasonal mean IWC with an increase of 1.0±1.2 % per decade. By converting the trend unit from g km^{-2}/dec to %/dec, the LIMA/Ice results also indicate an insignificant trend of $m = 2.15\pm2.44$ %/dec that is somewhat larger than the observed trend but agrees within the error bars.

So far, we have presented just single trends of ice water content (IWC). As has been discussed in Lübken et al. (2009) and Berger and Lübken (2011), temperatures in the summer mesopause region vary non-uniformly with time, mainly due to the influence of the temporal variation of ozone. Therefore, one might expect that a single linear trend is not the most appropriate method to represent trends in PMC over the entire period 1961–2013. Considering the time series of SBUV ozone anomalies (Fig. 5), we expect two potential break points in IWC trends around the years 1979 and 1997. We separate the entire period 1961–2013 into three time segments, namely 1961–1979, 1979–1997, and 1997–2013, and we separate the influence of different types of linear regression in

the trend estimation. The introduction of breakpoints clearly modifies the trends in IWC, yielding a much stronger trend for 1979–1996 than for 1961–2013. The dip in the ozone function at 1997 coincides with the deep solar minimum at 1997. Generally, all different trends derived from the three subperiods are statistical insignificant due the limited number of data, perhaps except for the periods 1979–1997 and 1997–2013 when using just simple linear regression. Our detailed multi-linear regression analysis shows that a period in the order of five decades is necessary to derive statistically significant trend estimations of IWC.

Summarizing, the microphysical ice model LIMA/Ice has proven to be a valuable tool to analyze long-term changes in various parameters of PMC. It turns out that trend in PMC depend on the latitude range, the PMC parameter considered, and the time period. The modeled PMC trends are caused by changes in mesospheric temperature and water vapor. Enhanced water vapor leads to stronger PMC formation. The linear trend in model temperatures at 83 km is rather small but significant with -0.58±0.32 K/dec at high latitudes in the period of 1961–2013.
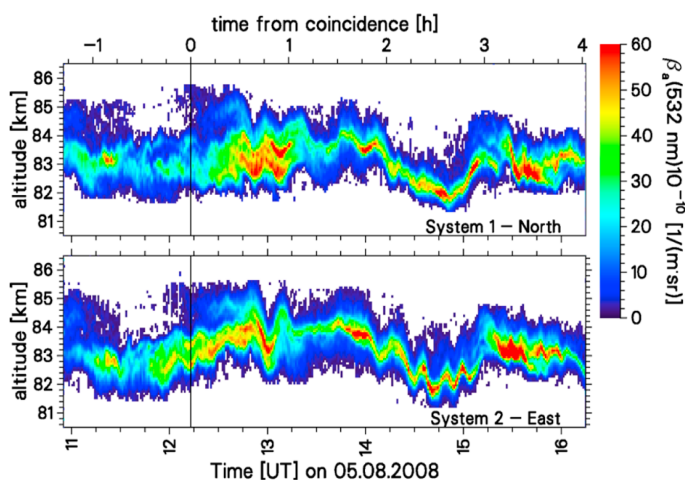
2.3.3   Lidar measurements

Figure 15: Temporal evolution of an noctilucent cloud (NLC) as observed by the two systems of the RMR-Lidar at ALOMAR. The line of sight is tilted 20° off zenith towards the East and the North. This plot is taken from Baumgarten et al. (2012).

In order to understand the processes involved in long-term variations of NLC and metal layers, we need to better understand the physics involved in the formation and modulation of these layers. This includes the potential impact of gravity waves on the morphology of NLC and metal layers. In Fig. 15 we show a high-resolution lidar measurement of an NLC layer which exhibits significant wave structure. We have performed model studies to better understand the impact of background parameters on the formation of NLC and the potential impact of non-spherical particle shape on the parameters deduced from lidar observations (*Kiliani et al.*, 2013, 2015).

Apart from long-term variations in MLT temperatures we study in detail trends in NLC. In Figure 16 we show our results regarding NLC occurrence at our institute in Kühlungsborn at 54°N (*Gerding et al.*, 2013a,b) It is obvious that occurrence rates show a significant anti-correlation with the solar cycle. This was expected since high solar activity enhances the dissociation of water vapor and heats the mesopause region, and both processes hinder the formation of ice particles (NLC). We find a very small and non-significant trend in occurrence rate of -0.1%/dec. Results from satellites published in the literature suggest a significant increase of NLC occurrence at mid-latitudes from 2002 to 2011, but miss the strong NLC reduction during the first part of solar cycle 23. It is interesting to note that our long-term observations of NLC at ALOMAR show practically no variation of NLC altitudes (**?**). Moreover, these NLC lidar altitudes agree surprisingly well with the historical

measurements from the late 19th century. Since NLC are very sensitive to temperatures (and water vapor), these observations pose a large constraints on the interpretation of long-term variations in the MLT.
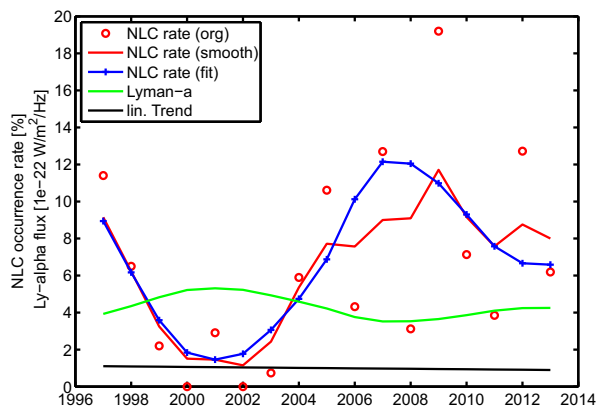

Figure 16: The occurrence rate of noctilucent clouds (NLC) at the IAP institute in Kühlungsborn (54°N). The dots show raw data whereas the solid lines show smoothed versions. The blue and black lines show a fit due to solar cycle modulation and trends, respectively. The green line shows the Ly-alpha variation (left axis) which is a good proxy for the solar cycle variation of solar activity.

2.3.4 Gravity waves and zonal momentum budget from radar measurements

Gravity waves (Gws) are of pivotal importance in the MLT since they drive the summer-to-winter-pole residual circulation which determines the cold summer polar mesopause and the warm stratopause in the polar night region. Due to a least a qualitative prevalence of gradient-wind balance in the MLT, the thermal structure induced by the residual circulation is associated with vertical shears of the mean zonal wind such as so refract the dominant gravity waves to break in a certain altitude regime. In order to quantify long-term variability in the MLT, it necessary to assess this *GW-mean flow interaction* on observational grounds. Our analysis of radar measurements has concentrated on inferring mean winds and vertical fluxes of horizontal momentum with respect to the annual cycle and year-to-year variations. In particular, we have aimed at the first quantitative verification of the momentum budget in the summer MLT by measurements. In following we summarize the main findings.

Momentum fluxes due to GWs are determined from the radial wind inferred from coplanar radar beams by applying the method of Vincent and Reid (1983). Our implementation of this method is described in detail in Placke et al. (2015a). It has been applied to the measurement period from 2008 to 20011 Placke et al. (2015b). Figure 17 shows height-time cross-sections of the 4-year means of the zonal wind (u) and the vertical flux of zonal momentum ($u'w'$). The zonal wind (upper panel) shows the well-known pattern with westward directed (negative) winds dominating during summer and eastward directed (positive) winds dominating during winter. Intra-seasonal variations occur during the winter months due to internal variability associated with quasi-stationary planetary Rossby waves. The transitions from winter to summer and from summer to winter occur typically during late March/early April and during in September. The wind reversal from westward to eastward winds with increasing altitude sets in May at about 100 km, and the zero wind line propagates downward reaching about 85 km in September.

The pattern of the momentum flux (lower panel in Fig. 17) confirms the strong dependence of GW propagation and breakdown on the background wind. This holds especially for the summer months when the vertical flux of zonal momentum is roughly anti-correlated with the mean zonal wind. There is flux of eastward momentum below and around the wind reversal followed by a
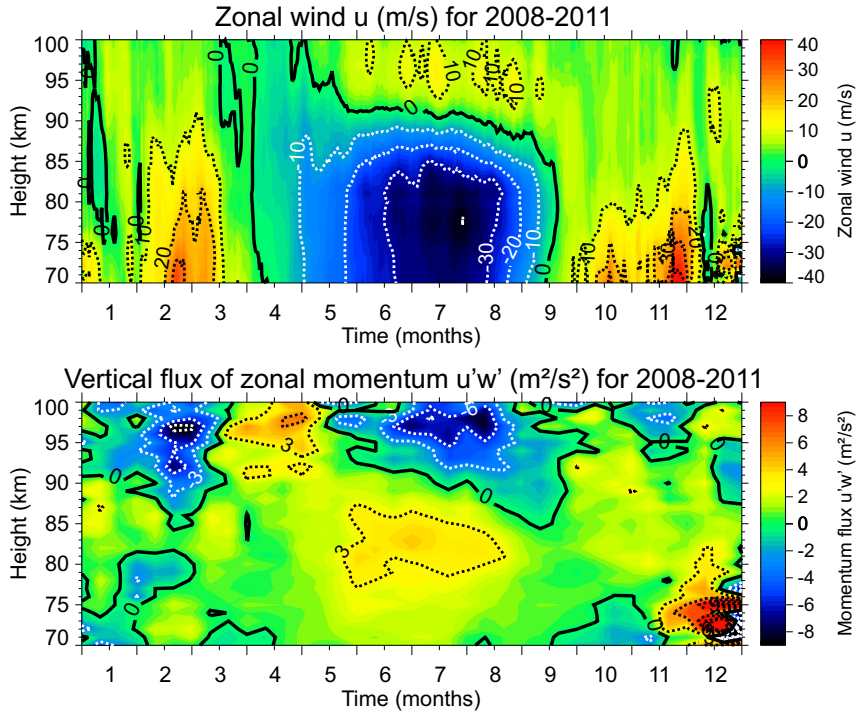
15

Figure 17: 4-year means of the zonal wind (top) and the vertical flux of zonal momentum (bottom) from the Saura MF radar. Zero contours are indicated by solid black lines. Dotted white and black lines denote contours for negative and positive values, respectively, with intervals of 10 m/s for wind and 3 m^2/s^2 for momentum flux. For further details see Placke et al. (2015a).

strong flux of westward momentum flux higher up. The latter feature is novel and not simulated in climate models. The strong vertical flux of westward momentum above the summertime wind reversal is strongly indicative of the generation of secondary GWs that propagate against the mean wind. These secondary waves are generated as a result of the breakdown of primary GWs that have propagated upward from their tropospheric sources. Such a process is excluded in standard GWs parameterizations, but shows up in the GW-resolving simulation with the KMCM discussed in the context of Fig. 4. In general, the averaged vertical flux of zonal momentum per unit mass varies between ± 9 m^2/s^2, which agrees with model estimates (e.g., Becker and von Savigny, 2010).

The momentum flux varies semi-annually around 90-100 km. That is, maximum (positive) values appear around the equinoxes with the major maximum in spring and a minor one in fall. During summer and winter, negative values dominate at these high altitudes. When considering altitudes around 70-80 km, the momentum flux is consistent with a semi-annual variation of GW activity with minima during equinox as was found in Hoffmann et al. (2010).

The zonal momentum budget in the summer MLT is dominated by the GW drag, D_u, and the Coriolis force associated with the mean meridional wind. In this sense, the mean meridional circulation (which in the summer MLT is approximately equal to the residual circulation) is *driven* by the breakdown of GWs. The balance can be written as $-f\,v \approx \rho^{-1}\,\partial_z\left(\rho\left(u'w'\right)\right) = D_u$, where f is the Coriolis parameter, v the mean meridional wind (as measured by the Saura radar), and ρ a reference density. The left panel of Fig. 18 shows vertical profiles averaged from June to August 2010 for the zonal wind, momentum flux, Coriolis force, and GW drag. Within the uncertainty of the observational data, the momentum budget is nicely fulfilled. We emphasize that this is the first observationally based quantitative account of the mean momentum budget in the summer MLT (where the temporal mean is representative of the zonal mean).

The momentum budget is complemented by a scatter plot (right panel) describing the correlation between $-f\,v$ and D_u based on 10-day averages of the underlying time series. The standard
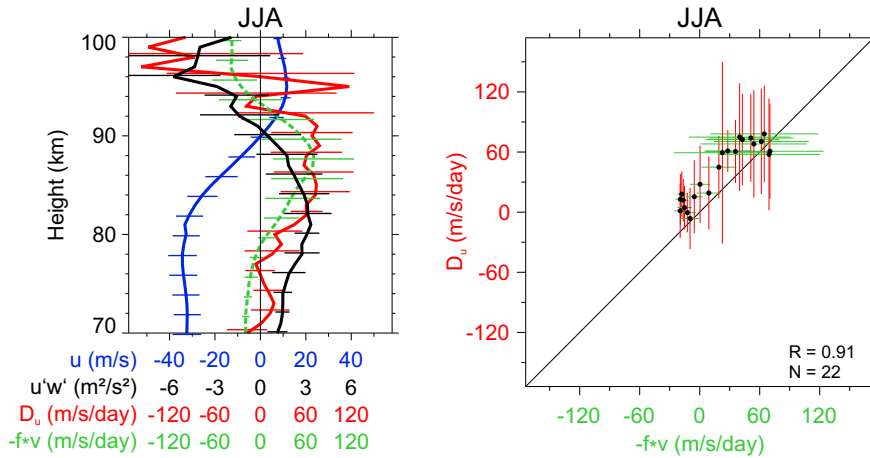
16

Figure 18: Left: Mean vertical profiles of mean zonal wind (blue), vertical flux of zonal momentum (black), GW drag (red), and negative Coriolis force (dashed green) based on Saura MF radar measurements in summer 2010. Horizontal lines denote standard deviations. Right: Scatter plot of negative Coriolis force and GW drag for the 71-92 km altitude regime, including the standard deviations. For further details see Placke et al. (2015b).

deviation of the zonal wind is about $7 \ \mathrm{m\,s}^{-1}$ below 90 km and 2-3 $\mathrm{m\,s}^{-1}$ farther above. The standard deviation of the momentum flux increases with height from about $1 \ \mathrm{m}^2\,\mathrm{s}^{-2}$ at 70 km to about $5 \ \mathrm{m}^2\,\mathrm{s}^{-2}$ at 100 km. Overall, these standard deviations mainly display internal variability and temporal evolution over the summer season.

The observationally obtained profile of the GW drag roughly consistent with model estimates. The maximum zonal-mean GW drag at 70^oN, averaged from June to August, in the KMCM is about 140 $\mathrm{m\,s}^{-1}\,\mathrm{d}^{-1}$ and located between 85 and 90 km. This holds for all model versions introduced in Sec. 2 (see also the discussion in Becker, 2012). Thus, there is a remaining quantitative discrepancy of about a factor of 2 between the GW drag as simulated in models and as deduced from state-of-the-art radar measurements. This issue needs to be resolved in the future. Also note that a complete assessment of the momentum budget requires to take traveling planetary waves and thermal tides into account.

3   Summary and perspective

The SAW project LOCHMES has given rise to significant progress in various ways concerning our knowledge about long-term changes in the middle atmosphere with focus on the mesosphere. We have strongly enhanced our modeling capabilities, and techniques for ground-based observations and data evaluation as well. New insight concerning global variability modes, long-term trends, annual and seasonal variations, and the influence of solar variability on the middle atmosphere has been obtained. Especially with respect to modeling the influence of the QBO and solar variability on the MLT, and regarding data analysis using the 3D residual circulation, a solid basis for further studies in this field at IAP has been provided.

References

Baldwin, M. P. and T. J. Dunkerton, 1998: Quasi-biennial modulation of the southern hemisphere stratospheric polar vortex. *Geophys. Res. Lett.*, **25 (17)**, 3343–3346, doi:10.1029/98GL02445.

Baumgarten, G., and J. Fiedler (2008), Vertical structure of particle properties and water content in noctilucent clouds, *J. Geophys. Res. Lett.*, *35*, L10811, doi:10.1029/2007GL033084.

Baumgarten, G., 2010: Doppler Rayleigh/Mie/Raman lidar for wind and temperature measurements in the middle atmosphere up to 80 km. *Atmos. Meas. Tech.*, **3**, 1509–1518, doi:10.5194/amt-3-1509-2010.

Baumgarten, G., A. Chandran, J. Fiedler, P. Hoffmann, N. Kaifler, J. Lumpe, A. Merkel, C. E. Randall, D. Rusch, and G. Thomas (2012), On the horizontal and temporal structure of noctilucent clouds as observed by satellite and lidar at ALOMAR (69N), *J. Geophys. Res. Lett.*, *39*, L01803, doi: 10.10.1029/2011GL049935.

Becker, E., 2009: Sensitivity of the upper mesosphere to the lorenz energy cycle of the troposphere. *J. Atmos. Sci.*, **66**, 647–666, doi:10.1175/2008JAS2735.1.

Becker, E., 2012: Dynamical control of the middle atmosphere. *Space Sci. Rev.*, doi:10.1007/s11214-011-9841-5.

*Becker, E., R. Knöpfel, and F.-J. Lübken, 2015: Dynamically induced hemispheric differences in the seasonal cycle of the summer polar mesopause. *J. Atmos. Sol.-Terr. Phys.*, **129**, 128–141, doi: 10.1016/j.jastp.2015.04.014.

Becker, E. and C. McLandress, 2009: Consistent scale interaction of gravity waves in the doppler spread parameterization. *J. Atmos. Sci.*, **66**, 1434–1449.

Becker, E. and C. von Savigny, 2010: Dynamical heating of the polar summer mesopause induced by solar proton events. *J. Geophys. Res.*, **115**, doi:10.1029/2009JD012561.

Berger, U., and F.-J. Lübken (2011), Mesospheric temperature trends at midlatitudes in summer, *J. Geophys. Res. Lett.*, *38*, L22804, doi:10.1029/2005GL024841.

DeLand, M. T., E. P. Shettle, G. E. Thomas, and J. J. Olivero (2007), Latitude-dependent long-term variations in polar mesospheric clouds from SBUV version 3 PMC data, *J. Geophys. Res. Atmos.*, *112*, doi:10.1029/2011GL049528.

DeLand, M. T., and G. E. Thomas (2015), Updated PMC Trends Derived from SBUV Data, *J. Geophys. Res. Atmos.*, *120*, 2140ï¿$\frac{1}{2}$-2166 doi:10.1002/2014JD022253.

Eixmann, R., M. Gerding, J. Höffner, and M. Kopp (2015), Lidars with narrow FOV for spectral and daylight measurements, *IEEE Transactions on Geoscience and Remote Sensing*, *53*, 4548–4553, doi: 10.1109/TGRS.2015.2401333.

Fasullo, J. T. and K. E. Trenberth, 2008: The annual cycle of the energy budget. part i: Global mean and land-ocean exchanges. *J. Clim.*, **21**, 2297–2312, doi:10.1175/2007JCLI1935.1.

Fomichev, V. I., W. E. Ward, S. R. Beagley, C. McLandress, J. C. McConnell, N. A. McFarlane, and T. G. Shepherd, 2002: Extended canadian middle atmosphere model: Zonal-mean climatology and physical parameterizations. *J. Geophys. Res.*, **107**, doi:10.1029/2001JD000479.

Gabriel, A., H. Körnich, S. Lossow, D. H. W. Peters, J. Urban, and D. Murtagh, 2011a: Zonal asymmetries in middle atmospheric ozone and water vapour derived from Odin satellite data 2001-2010. *Atmos. Chem. Phys.*, **11**, 9865–9885, doi:10.5194/acp-11-9865-2011.

Gabriel, A., H. Schmidt, and D. H. W. Peters, 2011b: Effects of the 11 year solar cycle on middle atmospheric stationary wave patterns in temperature, ozone, and water vapor. *J. Geophys. Res.*, **116 (D23301)**, doi: 10.1029/2011JD015825.

Gerding, M., J. Höffner, P. Hoffmann, M. Kopp, and F.-J. Lübken (2013a), Noctilucent cloud variability and mean parameters from 15 years of lidar observations at a mid-latitude site (54°N, 12°E), *J. Geophys. Res.*, *118*, 317–328, doi:10.1029/2012JD018319.

Gerding, M., M. Kopp, P. Hoffmann, J. Höffner, and F.-J. Lübken (2013b), Diurnal variation of midlatitude NLC parameters observed by daylight-capable lidar and their relation to ambient parameters, *Geophys. Res. Lett.*, *40*, 6390–6394, doi:10.1002/2013GL057955.

Gerding, M., K. Baumgarten, J. Höffner, and F.-J. Lübken (2015), Lidar soundings between 30 and 100 km altitude during day and night for observation of temperatures, gravity waves and tides, in *Reviewed and revised papers of the 27th International Laser Radar Conference, New York City, USA, 2015.*

Hansen, J., et al., 2005: Earth's energy imbalance: Confirmation and implications. *Science*, **308**, 1431–1435, doi:10.1126/science.1110252.

Hervig, M. E., and M. H. Stevens (2014), Interpreting the 35 year SBUV PMC record with SOFIE observations, *J. Geophys. Res. Atmos.*, *119*, 12,689–12,705, doi:10.1002/2014JD021923.

Hoffmann, P., E. Becker, W. Singer, and M. Placke, 2010: Seasonal variation of mesospheric waves at northern middle and high latitudes. *J. Atmos. Sol.-Terr. Phys.*, **72**, 1068 – 1079.

Hunten, D. M., R. P. Turco, and O. B. Toon (1980), Smoke and dust particles of meteoric origin in the mesosphere and stratosphere, *J. Atmos. Sci.*, *37*, doi:10.1175/1520-0469(1980)037h1342:SADPOMi2.0.CO;2.

*Karlsson, B. and E. Becker, 2015: Absolute interhemispheric coupling in the middle atmosphere. *J. Geophys. Res., submitted.*

*Kiliani, J. (2014) 3-D Modeling of Noctilucent Cloud Evolution and Relationship to the Ambient Atmosphere, *thesis*, Universität Rostock, Germany.

*Kiliani, J., G. Baumgarten, F.-J. Lübken, U. Berger, and P. Hoffmann (2013), Temporal and spatial characteristics of the formation of strong noctilucent clouds, *J. Atmos. Solar-Terr. Phys.*, *104*, 151–166, doi:10.1016/j.jastp.2013.01.005.

*Kiliani, J., G. Baumgarten, F.-J. Lübken, and U. Berger (2015), Impact of particle shape on the morphology of noctilucent clouds, *Atmos. Chem. Phys.*, *15*, 16,019–16,048, doi:10.5194/acp-15-16019-2015.

Kinoshita, T., Y. Tomikawa, and K. Sato, 2010: On the three-dimensional residual mean circulation and wave activity flux of the primitive equations. *J. Meteor. Soc. Japan*, **88**, 373–394.

*Knöpfel, R. and E. Becker, 2011: An idealized radiative transfer scheme for use in a mechanistic general circulation model from the surface up to the mesopause region. *J. Quant. Spectrosc. Radiat. Transfer*, **112**, 1460–1478, doi:10.1016/j.jqsrt.2011.02.014.

Lübken, F.-J., U. Berger, and G. Baumgarten (2009), Stratospheric and solar cycle effects on long-term variability of mesospheric ice clouds, *J. Geophys. Res. Atmos.*, *114*, D00I06, doi:10.1029/2009JD012377.

Lübken, F.-J., and U. Berger (2011), Latitudinal and interhemispheric variation of stratospheric effects on mesospheric ice layer trends, *J. Geophys. Res. Atmos.*, *116*, D00P03, doi:10.1029/2010JD015258.

Lübken, F.-J., U. Berger, and G. Baumgarten (2013), Temperature trends in the midlatitude summer mesosphere, *J. Geophys. Res. Atmos.*, *118*, doi:10.1002/2013JD020576.

Lübken, F.-J., J. Höffner, T. P. Viehl, B. Kaiffler, and R. J. Morris, 2014: Winter/summer mesopause temperature transition in 2011/2012 at Davis (69°S). *Geophys. Res. Lett.*, **41**, doi:10.1002/2014GL060777.

Lucarini, V. and F. Ragone, 2011: Energetics of climate models: Net energy balance and meridional enthalpy transport. *Rev. Geophys.*, **49 (RG1001)**, doi:10.1029/2009RG000323.

*Lübken, F.-J., J. Höffner, T. P. Viehl, E. Becker, R. Latteck, N. Kaiffler, D. Murphy, and and R. J. Morris, 2915: Winter/summer transition in the Antarcticmesopause region. *Geophys. Geophys. Res. Atmos.*, **120**, doi:10.1002/2015JD023928.

Manney, G. L., et al., 2008: The evolution of the stratopause during the 2006 major warming: Satellite data and assimilated meteorological analyses. *J. Geophys. Res.*, **113**, doi:10.1029/2007JD009097.

*Matthias, V. and E. Becker, 2015: Interhemispheric coupling induced by the holton-tan effect. *J. Geophys. Res., submitted.*

McFarlane, N. A., 1987: The effect of orographically excited gravity wave drag on the general circulation of the lower stratosphere and troposphere. *J. Atmos. Sci.*, **44**, 1775–1800.

McLandress, C., J. F. Scinocca, T. G. Shepherd, M. C. Reader, and G. L. Manney, 2013: Dynamical control of the mesosphere by orographic and nonorographic gravity wave drag during the extended northern winters of 2006 and 2009. *J. Atmos. Sci.*, **70 (7)**, 2152–2169, doi:10.1175/JAS-D-12-0297.1.

Meehl, G. A., J. M. Arblaster, J. T. Fasullo, A. Hu, and K. E. Trenberth, 2011: Model-based evidence of deep-ocean heat uptake during surface-temperature hiatus periods. *Nature Climate Change*, **1**, 360–364, doi:10.1038/nclimate1229.

Ortland, D. A. and M. J. Alexander, 2011: Gravity wave influence on the global structure of the diurnal tide in the mesosphere and lower thermosphere. *J. Geophys. Res.*, **111 (A10S10)**, doi:10.1029/2005JA011467.

Picone, J. M., A. E. Hedin, D. P. Drob, and A. C. Aikin, 2002: NRLMSISE-00 empirical model of the atmosphere: Statistical comparison and scientific issues. *J. Geophys. Res.*, **107 (1498)**, doi:10.1029/2002JA009430.

*Placke, M., P. Hoffmann, R. Latteck, and M. Rapp, 2015a: Gravity wave momentum fluxes from MF and meteor radar measurements in the polar MLT region. *J. Geophys. Res. Space Physics*, **120**, 736–750, doi:10.1002/2014JA020460.

*Placke, M., P. Hoffmann, and M. Rapp, 2015b: First experimental verification of summertime mesopsheric momentum balance based on radar wind measurements at 69° N. *Ann. Geophys.*, **33**, 1091–1096, doi:10.5194/angeo-33-1091-2015.

Sato, K., T. Kinoshita, and K. Okamoto, 2013: A new method to estimate three-dimensional residual-mean circulation in the middle atmosphere and its application to gravity wave-resolving general circulation model data. *J. Atmos. Sci.*, **70**, 3756–3779.

*Schlutow, M., E. Becker, and H. Körnich, 2014: Positive definite and mass conserving tracer transport in spectral GCMs. *J. Geophys. Res.*, **119**, doi:10.1002/2014JD021661.

Schmidt, H., G. P. Brasseur, and M. A. Giorgetta, 2010: Solar cycle signal in a general circulation and chemistry model with internally generated quasi-biennial oscillation. *J. Geophys. Res.*, **115 (D00I14)**, doi:10.1029/2009JD012542.

Senf, F. and U. Achatz, 2011: On the impact of middle-atmosphere thermal tides on the propagation and dissipation of gravity waves. *J. Geophys. Res.*, **116**, doi:10.1029/2011JD015794.

Shettle, E. P., M. T. DeLand, G. E. Thomas, and J. J. Olivero (2009), Long term variations in the 1071 frequency of polar mesospheric clouds in the Northern Hemisphere from SBUV, *J. Geophys. Res. Lett.*, *36*, L02803, doi:10.1029/2008GL036048.

Singer, W., R. Latteck, and D. A. Holdsworth, 2008: A new narrow beam Doppler radar at 3 MHz for studies of the high-latitude middle atmosphere. *Adv. Space Res.*, **41**, 1488–1494, doi:10.1016/j.asr.2007.10.006.

Viehl, T. P., J. Höffner, F.-J. Lübken, J. M. C. Plane, B. Kaifler, and R. J. Morris (2015), Summer time Fe depletion in the Antarctic mesopause region, *J. Atmos. Solar-Terr. Phys.*, pp. 97–102, doi:10.1016/j.jastp.2015.04.013.

Vincent, R. A. and I. M. Reid, 1983: HF Doppler measurements of mesospheric gravity wave momentum fluxes. *J. Atmos. Sci.*, **40**, 1321–1333.

von Savigny, C., S. V. Petelina, B. Karlsson, E. J. Llewellyn, D. A. Degenstein, N. D. Lloyd, and J. P. Burrows (2005), Vertical variation of NLC particle sizes retrieved from Odin/OSIRIS limb scattering observations, *J. Geophys. Res. Lett.*, *362*, L07806, doi:10.1029/2004GL021982.

Watanabe, S. and S. Miyahara, 2009: Quantification of the gravity wave forcing of the migrating diurnal tide in gravity wave-resolving general circulation model. *J. Geophys. Res.*, **114 (D07110)**, doi:10.1029/2008JD011218.

*Wolf, B., 2013: Parameterisierung orographischer schwerewellen. Diploma thesis, University of Rostock, 53 pp.